AIAA Journal
Vol. 55, No. 1, January 2017

Experimental Study of Flight Effects on Slightly Underexpanded Supersonic Jets

Benoît André,* Thomas Castelain,† and Christophe Bailly‡
École Centrale de Lyon, F-69134 Ecully Cedex, France

DOI: 10.2514/1.J054797

The flight effects on the properties of the mixing layer and the shock-cell system of slightly underexpanded supersonic jets are studied experimentally. Particle image velocimetry, schlieren visualizations, and pressure measurements are used in a dual-stream geometry whose outer flow simulates flight up to a Mach number of 0.4. The study of the mixing layer includes the evolution under simulated flight of the turbulence levels, the momentum thickness, and of integral length and time scales of turbulence. The turbulence levels are found constant in flight when defined as the ratio between peak velocity fluctuations and velocity difference across the mixing layer. The analysis of the shock-cell structure comprises an evaluation of flight effects on the length of the entire pattern, and on the length and strength of the individual shock cells. The shock-cell structure is stretched in flight, as well as each shock cell. This comes from the reduced mixing-layer growth occurring under flight conditions. The stretching of the pattern is accompanied by a decrease in strength of the first few shock cells.

Nomenclature

c	=	speed of sound
D	=	nozzle diameter
D_j	=	perfectly expanded jet diameter
IW_{begin}	=	starting size of the correlation windows in the MCCDPIV algorithm
IW_{end}	=	end size of the correlation windows in the MCCDPIV algorithm
i, j, k	=	variable numbers within (1, 2), 1 denoting the axial and 2 the radial component
$L_{ii}^{(k)}$	=	integral length scale of turbulence
L_s	=	shock-cell length
$\overline{L_s^f}$	=	mean shock-cell length in flight conditions
$\overline{L_s^g}$	=	mean shock-cell length in static conditions
M_c	=	convective Mach number of the shear layer
M_f	=	flight Mach number
M_j	=	perfectly expanded jet Mach number
M_r	=	relative Mach number of the shear layer
P_{amb}	=	ambient pressure
$P_{\max}$	=	maximum static pressure inside a shock cell
$P_{\min}$	=	minimum static pressure inside a shock cell
P_s	=	static pressure
q	=	ratio of the velocity of the subsonic flow over the one of the supersonic flow
R_{ij}	=	correlation coefficient of u
St	=	Stokes number
s	=	ratio of the density of the subsonic flow over the one of the supersonic flow
T_{cii}	=	integral timescale of turbulence in the convected frame
T_t	=	total temperature
t	=	time
U	=	scaling velocity
U_{exit}	=	jet velocity at the nozzle exit
U_j	=	ideally expanded flow velocity for the supersonic jet
$U_{\max}$	=	maximum jet velocity
U_p	=	mean velocity in the primary (supersonic) jet
U_s	=	mean velocity in the secondary (subsonic) jet
u	=	instantaneous velocity
x	=	longitudinal coordinate
$\boldsymbol{x}$	=	reference point of calculation of the correlation coefficient of u
y	=	transverse coordinate
y_i	=	inner boundary of the jet shear layer
y_o	=	outer boundary of the jet shear layer
β	=	shock parameter, $(M_j^2 - 1)^{1/2}$
Δt	=	time delay between two laser pulses
ΔU	=	mean velocity difference across the jet shear layer
δ_θ	=	shear-layer momentum thickness
$\boldsymbol{\xi}$	=	separation vector
ξ_p	=	particle relaxation distance
σ_i	=	rms value of u_i' or the radial maximum thereof at axial station x
τ	=	time delay in Eq. (5)
τ_f	=	fluid-mechanical timescale
τ_p	=	particle relaxation time
$\bar{\cdot}$	=	ensemble or time average of $\cdot$
$\cdot'$	=	fluctuating component of $\cdot$

I. Introduction

FLIGHT effects on jet noise have been extensively studied since the 1970s. There is indeed an interest in understanding the changes brought about by the external flow coming from the aircraft flight on the structure of the jet exhausted by the turbofan engines and on the emitted mixing noise. The goal is usually to tackle the issue of community noise. Most of the early studies combined theoretical developments and acoustic experiments [1,2], but some also presented aerodynamic measurements. For instance, Morris [3] investigated flight effects on subsonic and fully expanded supersonic jets by means of a laser Doppler velocimeter. His results were then used by Tanna and Morris [4] as inputs into a theory of flight effects on mixing noise. Larson et al. [5] also addressed many aspects of the turbulence of a subsonic jet with external stream using single- and two-probe hot-wire measurements, including mixing-layer growth, turbulence level, convection velocity, or integral length and time scales. They subsequently used these data to predict the relative velocity exponent, summarizing the overall mixing-noise reduction in flight.

Presented as Paper 2013-2079 at the 19th AIAA/CEAS Aeroacoustics Conference, Berlin, Germany, 27–29 May 2013; received 8 October 2015; revision received 3 June 2016; accepted for publication 3 June 2016; published online 23 August 2016.

*Postdoctoral Fellow, Univ Lyon, LMFA, UMR CNRS 5509, 36 Avenue Guy de Collongue.

†Assistant Professor, Univ Lyon, Université Lyon 1, LMFA, UMR CNRS 5509, 36 Avenue Guy de Collongue; thomas.castelain@ec-lyon.fr.

‡Professor, Univ Lyon, LMFA, UMR CNRS 5509, 36 Avenue Guy de Collongue. Senior Member AIAA.

The commercial aircraft powered by turbofan engines exhaust slightly underexpanded supersonic jets at cruise, characterized by the presence of a shock-cell pattern in the jet plume [6–8]. The interaction in the jet mixing layer between the turbulence and the shock-cell system is responsible for the so-called shock-associated noise, which comes in addition to the turbulent mixing noise. Shock-associated noise is made up of two distinct parts: a tonal one, referred to as screech [9,10], and a broadband one [11,12]. However, only the broadband component seems to be emitted in the practical, full-scale problem.

The use of composite materials in the fuselage of the next-generation aircraft, inducing lower sound-transmission losses than classical metallic structures, has raised concerns about the noise levels in the cabin. Hence, there is currently a renewed interest for studying the behavior of shock-associated noise in flight. Among the relevant works in the literature, Bryce and Pinker [13] showed that the shock cells of underexpanded jets lengthen with secondary flow. Sarohia [14] presented shadowgrams of supersonic jets in flight and acoustic measurements, with a study of the effect of the initial conditions on the jet. Norum and Shearin [15–17] performed extensive acoustic measurements as well as static-pressure surveys to determine the flight effects on the shock-cell structure and the shock-associated noise, up to a flight Mach number M_f of 0.4. Their study was extended to higher values of M_f by Norum and Brown [18]. In these works, no account of turbulence was given. More recently, Rask et al. [19] investigated a dual-stream configuration, in which the supersonic jet exhausted from a chevron nozzle, to understand the influence of this device on supersonic jet noise in flight. They measured the static pressure inside the jet and the noise emitted, applied particle image velocimetry (PIV), and presented turbulent kinetic energy profiles. Further data on turbulence in a shock-containing jet under flight conditions have been obtained in the present study, and could help modeling the supersonic jet noise in flight.

The present paper is organized as follows. Firstly, the experimental methods employed are presented. Secondly, the flight effects on mixing layer and shock-cell structure are deduced from PIV results, pressure measurements, and schlieren visualizations. Finally, concluding remarks and perspectives are proposed.

II. Experimental Methodology

A. Facility

The dual-stream facility employed for the present study was described previously in [20].

An underexpanded supersonic jet flow (also called primary jet in the following) originates from a continuously operating compressor mounted upstream of an air drier. Two contoured convergent nozzles are used. One is a round nozzle of diameter 38.25 mm. It will be referred to as the plain nozzle in the following. The second one has a diameter of 38.7 mm and has shallow notches cut into its lip. It is called hereafter notched nozzle. It has been shown that this nozzle nonintrusively suppresses screech [21]. In the following, the nozzle diameter of the supersonic jet is called D, whatever the nozzle is. To better simulate the conditions arising in air transport, most of the results presented here have been obtained with the screech-suppressing nozzle, in particular the entire turbulence data from the PIV. The plain nozzle was mounted for the static-pressure measurements, and given that the presence of the pressure probe prevents screech noise for the operating conditions presented, the conclusions reached are believed to be also valid in the case of the screech-suppressing nozzle; see Sec. IV. D. The reservoir temperature T_t is measured upstream of the exit. Here, the jets are unheated and $T_t \approx 30°\mathrm{C}$. The nozzle pressure ratio (NPR), defined as the ratio between jet stagnation pressure and ambient pressure, is set by measuring the wall static pressure 15 nozzle diameters upstream of the exit. In the following, results for jets of ideally expanded Mach number $M_j = 1.10$ and 1.15 are presented, corresponding to NPR $= 2.14$ and 2.27, respectively. The shock parameter $\beta = \sqrt{M_j^2 - 1}$ will also be used. The values of β for the jets under study are 0.46 and 0.57.

A subsonic jet (also called secondary jet in the following) is generated by a fan, and it exhausts through a 200-mm-diam contoured convergent nozzle. Well upstream of the exit, the supersonic duct penetrates into the subsonic flow. In the final section before the exit, both ducts are cylindrical and coaxial, and the two jets have the same exit plane, with the subsonic jet flowing around the supersonic jet. The adequacy of the ratio between the supersonic and subsonic jet diameters for flight simulation has been checked in [20]. The Mach number of the subsonic jet, or flight Mach number, written M_f, can be varied from 0 to 0.4 approximately. Results are obtained for $M_f = 0$ (or 0.05 for PIV, see the following), 0.22, and 0.39.

B. Schlieren Imaging and Static-Pressure Measurements

A conventional Z-type schlieren system is used to visualize the flow. It consists of a light-emitting diode as light source, two 203.2-mm-diam $f/8$ parabolic mirrors, a straight knife-edge set perpendicular to the flow direction, and a high-speed CMOS Phantom V12 camera. The schlieren pictures presented hereafter illustrate thus the density gradients along the jet-axis direction.

Static-pressure measurements are performed by means of short probes based on a design by Pinckney [22]. They have an outer diameter of 1.5 mm and a tip to static hole distance smaller than 5 mm. Their compact geometry aims at solving the difficulty of measuring pressure in a flow with high gradients. Such probes have been extensively used for shock-cell-structure characterizations, especially in connection with broadband shock-associated noise (BBSAN) [17,23]. Some of our results have been compared with static-pressure profiles by Norum and Seiner [23], and a good agreement has been found [8].

C. Particle Image Velocimetry

PIV is also applied to the jets exhausting from the notched nozzle. The material involved and the setup are now detailed. Particle images are acquired using a pair of Phantom V12 cameras of sensor size $1280 \times 800\ \mathrm{px}^2$ mounted according to the Scheimpflug criterion, thus permitting the images to be focused across their entire width. Using a pair of cameras allows us to double the axial field of view, which covers a length of about two jet diameters. In the radial direction, due to the axisymmetric character of the jet and the emphasis laid on the investigation of the mixing layer, the field of view extends from below the jet centerline up to a distance of about $1.5D$ from it (see Fig. 1). The PIV setup is mounted on a frame, which can be translated in the jet direction; an axial extent of $12D$ is studied here, meaning that the entire field has been acquired in six parts. For each new location of the frame, a calibration of the images is performed using a three-dimensional LaVision plate, the jet operating conditions are reset, and 2000 image pairs are recorded. The acquisition frequency of the image pairs is 500 Hz. The delay between the images of each pair is set to $\Delta t = 3\ \mu\mathrm{s}$ for all jet conditions. The cameras are fitted with 135 mm Nikkor-Q lenses set at an aperture of $f/2.8$. The magnifying factor for each camera is about 0.05 mm/px. Velocity is measured in a plane containing the jet axis and a notch of the nozzle. Illumination is provided by a pulsed double-cavity Nd:YLF Quantronix Darwin-Duo laser at 527 nm wavelength, with 18 mJ pulse energy (at 1000 Hz discharge frequency). The duration of a pulse amounts to 120 ns. The sheet thickness is 1.7 mm (± 0.3 mm). The supersonic jet is seeded with olive oil by means of custom-designed Laskin nozzle generators; the mean particle size was experimentally determined to be around 1 μm [7]. The subsonic flow is seeded by smoke. The static condition ($M_f = 0$) is replaced by a minimum flight Mach number of 0.05 to ensure seeding of the supersonic-jet surroundings. Both seeding devices are mounted far enough upstream of the exit so that the particle concentration in each flow is approximately uniform.

These parameters, and others of interest, which can be derived from them, are gathered in Table 1. In particular, some optical features are estimated from Raffel et al. [24]. Considering the maximum jet velocity and the optical resolution of the images, the motion of a particle over the duration of a laser pulse can be calculated to be at most 1 px, thus preventing any blurring effect. Investigation of the particle images showed that the real particle-image size reached a few pixels.

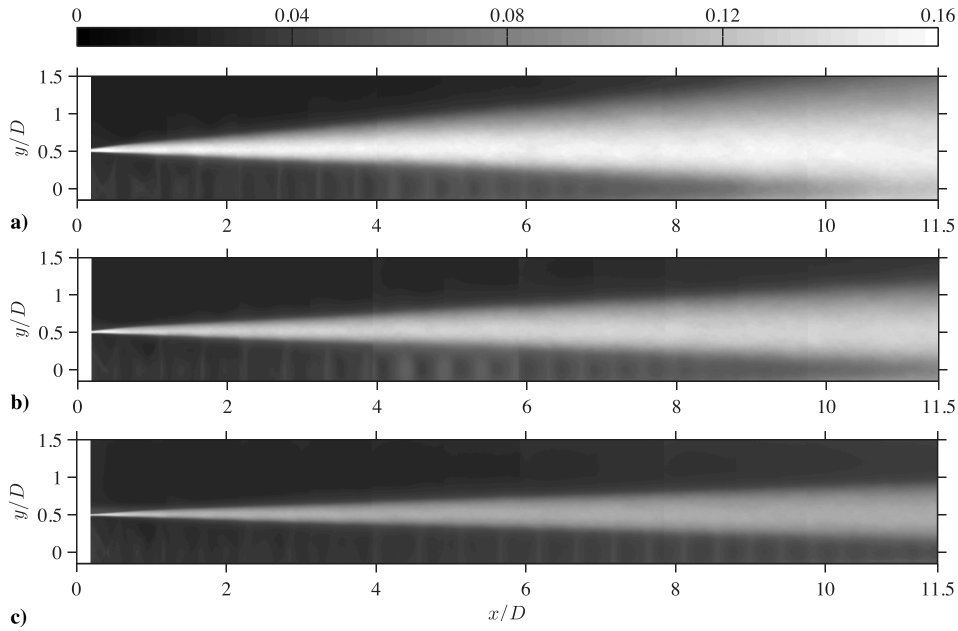

Fig. 1 Cartography of σ_1/U_j, at $M_j = 1.10$ and a) $M_f = 0.05$, b) $M_f = 0.22$, and c) $M_f = 0.39$.

The postprocessing choices are now mentioned. Vector-field calculation is performed by the MCCDPIV algorithm of the LaVision DaVis 7.2 software. In all but the last iteration, the calculation is a two-inner-iteration process; a 25% overlap of the interrogation windows is set and no window ponderation is used. For the last iteration, three inner iterations are set, as well as a 50% overlap and an isotropic Gaussian window ponderation. The initial correlation windows are of size $IW_{\text{begin}} = 64 \times 64\ \text{px}^2$ and the final ones of size $IW_{\text{end}} = 8 \times 8\ \text{px}^2$, leading to a vector density of one every 0.2 mm, or approximately 190 vectors across the supersonic-jet diameter. The algorithm is applied individually to each set of 2000 images recorded by each camera at one axial location. Stitching of the 12 velocity fields for each jet occurs afterward, if necessary, through a MATLAB script. When possible, however, depending on the analysis wanted, the velocity fields are not interpolated prior to postprocessing. The velocity fields are filtered after each iteration of the multigrid algorithm apart from the last one by a detectability filter (threshold of 1.05) and a median filter. Deleted vectors are replaced by interpolation. The final vectors coming from the last iteration are not filtered in DaVis. Several treatments were tested, and the Chauvenet criterion was finally applied to them (see [25], for example): this criterion works similarly to the median filter, but instead of comparing a vector with its neighbors in space, it does so with its neighbors in time. A vector is rejected if one of its values of axial or radial component is thought to be too far away from the mean, the allowed distance depending on the size of the statistical population. This criterion was found to nicely clean up the profiles of fluctuating velocity, especially in the jet core [8]. In the following, all PIV data are deduced from velocity fields filtered by the Chauvenet criterion apart from the length scales $L_{ii}^{(k)}$ and the timescales T_{cii}. The influence of the filter on $L_{ii}^{(k)}$ was found to be negligible, and T_{cii} is directly derived from $L_{ii}^{(k)}$ through Eq. (7). The relevance of the $8 \times 8\ \text{px}^2$ final window size with regard to the signal-to-noise ratio was tested against results obtained $IW_{\text{end}} = 16 \times 16\ \text{px}^2$. Even at a more difficult condition than the ones considered here ($M_j = 1.50$), the velocity fluctuations were found to be close between the two computations, as were the turbulence length scales. The choice of final window sizes of $8 \times 8\ \text{px}^2$ was motivated by the strong gradients observed in the jets under study, making it critical to have a small final interrogation window to minimize spatial averaging.

Table 1 Material-related PIV parameters (* in the mixing layer)[a]

Parameter	Value	Relative value
Sheet thickness	1.7 mm	$0.04D$
Total field of view	$449 \times 67\ \text{mm}^2$	$11.6D \times 1.73D$
Δt	3 μs	—
Magnification	0.05 mm/px	$0.0013\,D/\text{px}$
Maximum interimage displacement*	16 px	$0.02D$
Diffraction-limited particle diameter	5 μm	0.25 px
Depth of field	0.27 mm	$0.007D$

[a]Some optical parameters have been calculated using formulas from [24].

Applying PIV to imperfectly expanded supersonic flows entails several challenges related to the particle response to high flow gradients [26]. The behavior of the seeding particles in such flows was studied in [7] from laser Doppler velocimetry (LDV) data. Here, Stokes number estimates, written *St*, are proposed. Adopting the methodology of Mitchell et al. [27], the particle relaxation time τ_p is derived from a LDV traverse on the centerline of a jet at $M_j = 1.50$, showing a Mach disk. The relaxation time after the step change due to the strong shock can be estimated to be 2.9 μs, corresponding to a relaxation distance ξ_p of 1.1 mm. To form the Stokes number, the ratio of τ_p over a fluid-mechanical timescale τ_f has to be built. Many expressions for τ_f exist in the literature. For instance, Nouri and Whitelaw [28] use $D/U_{\max}$, $U_{\max}$ being the maximum velocity in the jet. Mitchell et al. [27] propose D/U_{exit}, U_{exit} being the flow velocity at the nozzle exit. Edgington-Mitchell et al. [26] use L_s/U_{exit}, with L_s the shock-cell spacing. Another possible timescale, which is more related to the mean-velocity fluctuations engendering particle lag, could be $1/\max(\nabla \bar{u})$, in which $\max(\nabla \bar{u})$ stands for the maximum velocity gradient encountered along the streamlines. The latter is about $10\ \text{m} \cdot \text{s}^{-1} \cdot \text{mm}^{-1}$ in the investigated jets. (Incidentally, this makes clear that the jets under study do not present strong shocks associated with velocity discontinuities.) Interestingly, all these estimations lead to a value of τ_f around 0.1 ms, hence

$$St = \frac{\tau_p}{\tau_f} \approx 0.03 \tag{1}$$

The traditional criterion $St \ll 1$ is thus satisfied. Alternatively, the spatial and temporal ratios [29]

$$SR = \frac{IW_{\text{end}}}{\xi_p} \quad \text{and} \quad TR = \frac{\Delta t}{\tau_p} \tag{2}$$

can be formed. They have a value of 0.38 and 1, respectively, with the present setup, which is in the correct range after Ragni et al. [29]. The

Table 2 Multigrid and particle-response parameters

Parameter	Value
IW_{begin}	64 px
IW_{end}	8 px
ξ_p	1.1 mm
τ_p	2.9 μs
SR [29]	0.38
TR [29]	1.0
St	0.03

multigrid and particle-response parameters are summarized in Table 2.

Finally, the PIV results were checked to have a good statistical convergence and repeatability. The absence of peak locking was ensured by scrutinizing the homogeneity between 0 and 1 of the fractional part of the calculated displacements expressed in pixels, and this over entire fields. Also, the mean-velocity results obtained by PIV were compared to LDV profiles, and a good agreement was found [8].

III. Flight Effects on the Mixing Layer

The analyses performed in the following are detailed in [30], so that only a brief account of the data-reduction procedures is provided here. In the following, the origin of the coordinates is taken at the center of the mounted primary nozzle. The variable x denotes the longitudinal direction and y the transverse direction.

A. Turbulence Levels

1. Data Reduction and Results

To begin with, the effect of flight on the turbulence levels in the mixing layer is estimated. Cartographies of the longitudinal rms velocity fluctuations are shown in Fig. 1, in which M_f is increased from $M_f = 0.05$ to 0.39 for $M_j = 1.10$ (notched nozzle). The absolute levels of velocity fluctuations decrease in flight, which comes from the reduced mean-velocity shear when M_f is increased.

In the following, $\sigma_i(x)$ will denote the peak value along a radial line at x constant of the rms velocity fluctuations, with $i = 1$ for the axial-velocity component and 2 for the radial one. Turbulence being mainly produced by velocity gradients, the ratios of the σ_i over the velocity difference ΔU between the supersonic jet and the low-speed coflow are used as indicators of turbulence levels. Because underexpanded supersonic jets are not uniform, it is not obvious which velocity is to be considered to calculate ΔU. A mean velocity, noted U_p (for primary jet), is chosen here, about which the axial velocity oscillates in the shock-cell structure. ΔU is then defined as $U_p - U_s$, with U_s the secondary-jet velocity. The value of ΔU is thus taken constant, independent on the axial station x.

The flight effects on the peak turbulence levels in the mixing layer are presented in Fig. 2 for $M_j = 1.10$ and 1.15. In each plot, the three upper curves show σ_1, whereas the three lower ones correspond to σ_2. Nondimensioned by ΔU, the peak fluctuation levels are almost constant with M_f, apart in a region near the nozzle exit.

In the literature, there is no consensus on the effects of a secondary flow on the absolute fluctuation levels. For the sake of clarity, the literature review is separated between papers handling the developed region and those focusing on the initial jet, and is followed by a discussion.

2. Developed Region

Goebel and Dutton [31] measured turbulence properties in the fully developed region of several plane, compressible mixing layers using a two-component laser Doppler velocimeter. They found that $\sigma_1/\Delta U$ did not depend on the relative Mach number of the mixing layer M_r, and that $\sigma_2/\Delta U$ decreased when M_r increased. Translated into the present problem, this means that $\sigma_1/\Delta U$ should remain constant, and that $\sigma_2/\Delta U$ should increase when M_f is increased. Morris [3] obtained a dependence of the peak longitudinal fluctuation intensity σ_1/U_p on the flight velocity reading $(1 - U_s/U_p)^{0.7}$, whereas the present results lead to a proportionality of the same ratio with $(1 - U_s/U_p)^1$. Interestingly, the exponent 0.7 was also obtained by Larson et al. [5].

According to Morris [3], the reason for these discrepancies should be the variations in initial conditions. Indeed, he hypothesized that his exponent 0.7 should be specific to the experimental facility, and stated that, if it were not for the influence of the initial conditions, a linear dependence on the velocity difference should prevail, as it is the case in the present study.

3. Initial Development

Sarohia and Massier [32] showed by schlieren visualizations and jet-noise measurements that the thickness of the boundary layer on the outer side of the primary jet had an influence on the effects of flight. According to them, this external boundary layer leads to a situation, in which it is as if there was no external flow, at least near the nozzle-exit plane. Therefore, turbulence should scale with a velocity greater than ΔU (and smaller than the jet velocity) on an axial extension depending on this initial boundary-layer thickness. Returning to the results shown in Fig. 2, it has already been pinpointed that the curves do not collapse in the initial portion of the mixing layer. More precisely, the turbulence levels increase with M_f. To obtain constant turbulence levels in the initial portion of the shear layer, the absolute levels of rms velocity would have to be divided by another velocity scale U, U being greater than ΔU for $M_f = 0.05$ and 0.22. Choosing $U = U_p$ as the reference velocity reverses the trend and makes the turbulence levels decrease with M_f. This means that the scaling velocity U should be between ΔU and U_p in the initial portion of the jet, which is quite in agreement with the proposition by Sarohia and Massier [32].

4. Discussion

The argument of the external boundary layer can explain the peculiar behavior of the turbulence levels in the initial jet development. It seems, however, hard to believe that the external boundary-layer

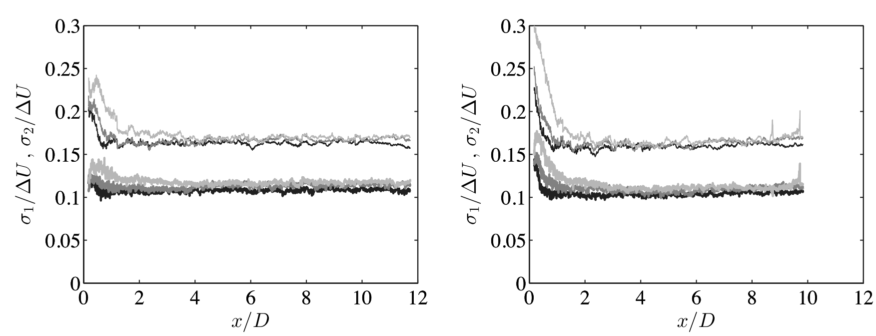

a) b)

Fig. 2 Peak turbulence levels: a) $M_j = 1.10$, b) $M_j = 1.15$; black lines: $M_f = 0.05$, dark-gray lines: $M_f = 0.22$, light-gray lines: $M_f = 0.39$; —, —, — (thin lines) $\sigma_1/\Delta U$; ━, ━, ━ (thick lines) $\sigma_2/\Delta U$.

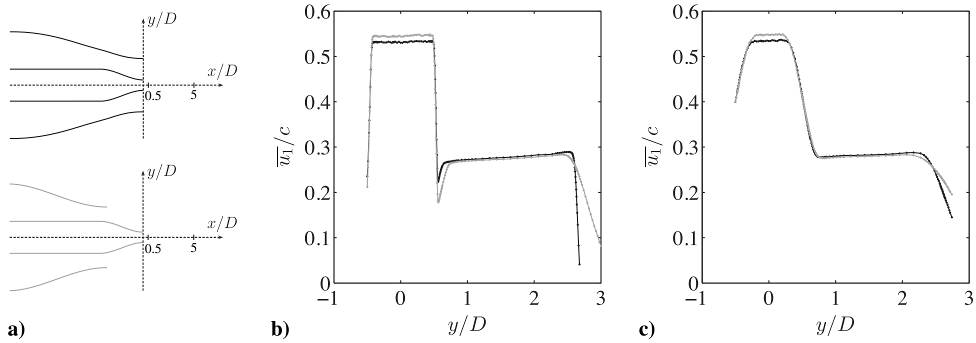

Fig. 3 Radial profiles of $\overline{u_1}/c$ measured for two different secondary nozzles (color coding like in the sketch in a), for $M_j = 0.55$ and $M_f = 0.27$, at b) $x/D = 0.5$, c) $x/D = 5$.

thickness have such an influence on the entire mixing-layer development. Another candidate for explaining why the turbulence levels should behave differently between the different studies could be the radial mean-velocity profile of the external flow. In the facility of Morris [3], the primary jet is placed inside a large wind tunnel. Considering the section area of the secondary flow in such a facility, it increases next to the primary-jet nozzle exit because of the outer shape of the primary nozzle. This may lead to a mean-velocity deficit in the secondary flow near the supersonic jet, which could have a longer-lasting effect than the external boundary-layer thickness. The test was made in the current facility with another secondary-jet nozzle whose exit section is located approximately $3.5D$ upstream of the supersonic-jet exit. Radial profiles of axial velocity were measured using a Pitot probe. The comparison between the baseline secondary nozzle and the shorter one is shown in Fig. 3 for two axial stations, along with a sketch to scale of both arrangements considered. (The plain nozzle was used for the primary jet.) In Fig. 3, the axial velocity has been normalized by the local speed of sound c. Although the velocity deficit is clearly visible on the upstream profile at $x = 0.5D$, it utterly disappears by $5D$. (The small difference in the velocity of the primary jet, operated for this test at a subsonic condition, is immaterial for this analysis.) Hence, the variation in the relative location of primary-jet and secondary-jet exit planes between the various experimental arrangements may not have a decisive effect on the mean-velocity profile across the mixing layer. As a consequence, it is not clear what the reason is for the disparity in the turbulence results between the studies mentioned and the present one.

B. Momentum Thickness

The mixing-layer momentum thickness is defined as

$$\delta_\theta = \frac{1}{[\overline{u_1}(y_i) - \overline{u_1}(y_o)]^2} \int_{y_i}^{y_o} [\overline{u_1}(y) - \overline{u_1}(y_o)][\overline{u_1}(y_i) - \overline{u_1}(y)]\,\mathrm{d}y \quad (3)$$

in which u_1 is the axial-velocity component, y_i and y_o are the inner and outer mixing-layer boundaries, and the overline denotes the ensemble averaging operator. So as to properly define these boundaries, the fluctuation data obtained by the PIV are used. For each axial station, the radial location of the maximum of σ_1 is determined. In the high- and low-velocity sides of the mixing layer, the fluctuation minima are searched. For each side, the mixing-layer boundary is defined as the location where the rms velocity has decreased to 0.1 times the difference between the maximum and the minimum of the fluctuations. Finally, the integration of Eq. (3) is performed between these two limits.

The evolution of δ_θ/D along the mixing layer for $M_j = 1.10$ and the three values of M_f is shown in Fig. 4, only as far downstream as the inner boundary of the layer does not reach the jet axis (i.e., until the end of the potential core). Firstly, the mixing-layer growth is linear for all jets, which is characteristic of fully turbulent mixing layers [33]. Secondly, the growth rate decreases when M_f is increased. This is a well-known effect of the presence of a secondary stream, coming from the reduced shear across the mixing layer. It was

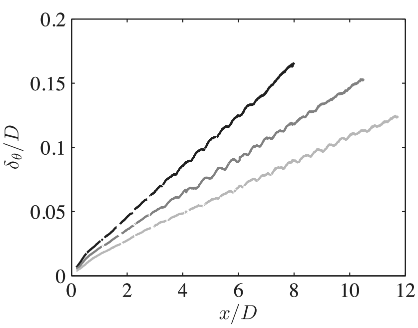

Fig. 4 Evolution of δ_θ/D along the mixing layer at $M_j = 1.10$; — $M_f = 0.05$, — $M_f = 0.22$, — $M_f = 0.39$.

already clearly visible in Fig. 1. The growth-rate decrease or its consequences have already been shown by velocity measurements [3,5,34], or schlieren visualizations [14,32]. It entails a stretching of the entire flow and in particular a lengthening of the potential core. The numerical values of the growth rates $\mathrm{d}\delta_\theta/\mathrm{d}x$, slopes of the straight lines fitting the calculated data, are given in Table 3 for $M_j = 1.10$ and 1.15.

To check the adequacy of the present mixing-layer growth rates with the literature, our values can be compared to typical experimental results obtained for compressible mixing layers. Classically, the growth rate $\mathrm{d}\delta/\mathrm{d}x$ is expressed as [35,36]

$$\mathrm{d}\delta/\mathrm{d}x = \delta'_{\mathrm{ref}} \frac{(1-q)(1+\sqrt{s})}{2(1+q\sqrt{s})} \Phi(M_c) \quad (4)$$

in which q (respectively, s) is the ratio of the velocity (respectively, density) of the subsonic flow over the supersonic one, M_c is the well-known convective Mach number, Φ is a function representative of the compressibility effects (with $\Phi(0) = 1$), and δ'_{ref} is a proportionality constant depending on the way of establishing the thickness. In our jets, M_c is around 0.5 or lower. As the mixing-layer thickness is deduced here from velocity measurements, the so-called Langley curve can be used for estimating Φ, as recommended by Smits and Dussauge [36]. Concerning the proportionality constant δ'_{ref}, Goebel and Dutton [31] used 0.165 for a thickness resembling the estimate $y_o - y_i$, which has been found here to be 7.5 larger than δ_θ. Hence, $0.165/7.5$ is retained as the proportionality factor. In the end, the ratio of the left-hand side of Eq. (4) to its right-hand side has been computed for our jets, and the values are written in Table 4. All these

Table 3 Mixing-layer growth rates ($\mathrm{d}\delta_\theta/\mathrm{d}x$) as a function of M_j and M_f

	$M_f = 0.05$	$M_f = 0.22$	$M_f = 0.39$
$M_j = 1.10$	0.0199	0.0139	0.0101
$M_j = 1.15$	0.0175	0.0125	0.0091

Table 4 Ratios of the left-hand side of Eq. (4) to its right-hand side, as a function of M_j and M_f

	$M_f = 0.05$	$M_f = 0.22$	$M_f = 0.39$
$M_j = 1.10$	1.14	1.09	1.17
$M_j = 1.15$	1.02	0.97	1.04

ratios are clearly close to one, which demonstrates the consistency of the present growth rates with the literature.

C. Spatial Correlations

Spatial correlations are computed from the velocity fields to obtain information on the size of large turbulent structures. The coefficient of space–time correlation is written

$$R_{ij}(\boldsymbol{x}, \boldsymbol{\xi}, \tau) = \frac{\overline{u_i'(\boldsymbol{x}, t) u_j'(\boldsymbol{x} + \boldsymbol{\xi}, t + \tau)}}{\sigma_i(\boldsymbol{x}) \sigma_j(\boldsymbol{x} + \boldsymbol{\xi})} \tag{5}$$

in which the indexes i and j represent the velocity component, $\cdot'$ denotes the fluctuations of $\cdot$, $\boldsymbol{x}$ marks the position of the reference point, $\boldsymbol{\xi}$ is the separation vector, t is the time, and τ is the time delay. Ensemble averages are calculated over the 2000 fields acquired. In the following, only spatial correlations are computed ($\tau = 0$).

Cross correlations R_{11} and R_{22} have been estimated while moving the reference point on the axial line $y/D_j = 0.5$, with D_j the fully expanded jet diameter, slightly larger than D. This is done to account for the expansion of underexpanded jets. It has been checked, however, that the precise location of the reference points had only a marginal influence on the results. Correlation-coefficient maps can be found in [30].

From R_{ii}, $i \in (1, 2)$, it is possible to calculate the integral length scale of u_i' in the direction k, $k \in (1, 2)$, by

$$L_{ii}^{(k)}(\boldsymbol{x}) = \frac{1}{2} \int_{-\infty}^{+\infty} R_{ii}(\boldsymbol{x}, \xi_k) \, \mathrm{d}\xi_k \tag{6}$$

in which ξ_k is the separation distance in the direction k. In practice, the integration is performed over a finite interval. Here, it is done until the correlation contour of level 0.1 is reached, to avoid the low correlation domain, which can be noisy; in any case, the integration limit has little influence on the numerical values, and it has to be noted that integral length scales are merely order-of-magnitude estimates.

The evolution of $L_{11}^{(2)}/D$ along the mixing layer is shown in Fig. 5 for $M_j = 1.10$ and the three values of M_f. As expected, the integral length scale decreases with M_f, because the mixing layer becomes thinner. The ratio of $L_{11}^{(2)}$ with δ_θ is shown in Fig. 6, and a constant value is reached after a few diameters. This statement remains true for $M_j = 1.15$ and other integral length scales. The proportionality between the integral scales and the mixing-layer width is in agreement with the hot-wire measurements by Larson et al. [5] in an incompressible coaxial jet. It also seems here that the length scales become slightly larger with respect to δ_θ when M_f is increased. To summarize the tendencies obtained, the ratios between the growth rates of the scales $L_{ii}^{(j)}$ and the growth rates of δ_θ are shown in Table 5. The length $L_{22}^{(2)}$ is not included because the results are noisier for this scale. It is clear that the ratios increase with M_f (i.e., for smaller compressibility effects), in agreement with the partial results shown in Fig. 6. Considering the tendencies at fixed M_f, the ratios also rise with M_j, although the flow compressibility increases. Hence, compressibility alone cannot explain all the trends. However, another factor may be relevant as well for the evolution with increasing M_j: the degree of underexpansion is changed. Beside compressibility, the strength of the shock-cell pattern might, therefore, also be important in determining the integral length scales.

In [30], the shapes of the correlation contours are also analyzed. To that end, ellipses are fitted to them, and their geometrical parameters, like the size of axes and the inclination, are deduced. Such a procedure was also applied to the present jets, but no flight effect on these parameters could be found, and so these results are not shown here.

D. Integral Timescales in the Convected Frame

Integral timescales of turbulence in the convected frame measure the time a turbulent structure remains coherent in its motion. This is a significant piece of information, especially for BBSAN. Indeed, an important concept in the BBSAN models proposed by Harper-Bourne and Fisher [11], Tam and Tanna [12], and Tam [37] is the existence of interferences between partially coherent sound sources, which arise from the turbulent structures remaining self-correlated over several shock cells.

The timescales of turbulence can be computed directly from space–time correlation coefficients. The latter are not accessible from our PIV data though, because of the technical limitations of the PIV system regarding the acquisition rate. Following Fleury et al. [38], the integral timescale in the convected frame based on the fluctuating velocity in the direction i, T_{cii}, is estimated by

$$T_{cii} \approx \frac{L_{ii}^{(1)}}{\sigma_i} \tag{7}$$

It has to be noted that only the integral length scales in the axial direction (1), the direction of advection, are considered to build T_{cii}. To compute T_{cii}, the maximum of σ_i for each axial station is considered. The effect of flight on T_{c11} is given in Fig. 7 for $M_j = 1.10$. The flight Mach number is found to have no effect on the turbulence timescale in the convected frame. The decreases in $L_{11}^{(1)}$ and σ_1 compensate each other to leave T_{c11} unchanged when M_f is increased. This statement is also true for T_{c22}. Moreover, the jet at $M_j = 1.15$ behaves in the same way (not shown here). Note that the relation proposed by Larson et al. [5], $T_c \propto \delta_\theta/\Delta U$, is compatible with the present conclusion.

IV. Flight Effects on the Shock-Cell Structure

A. Flight Effects on the Entire Length of the Shock-Cell Structure

The entire shock-cell structure of three jets at $M_j = 1.15$ with increasing flight Mach number is shown by means of schlieren visualizations in Fig. 8. (Each picture of the figure is made up of

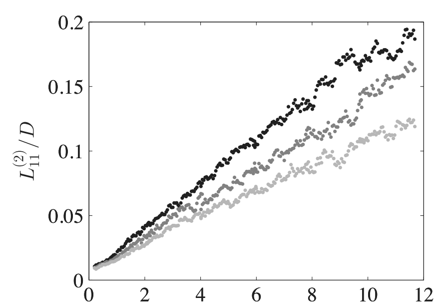

Fig. 5 Evolution of $L_{11}^{(2)}/D$ along the mixing layer, $M_j = 1.10$; • $M_f = 0.05$, • $M_f = 0.22$, • $M_f = 0.39$.

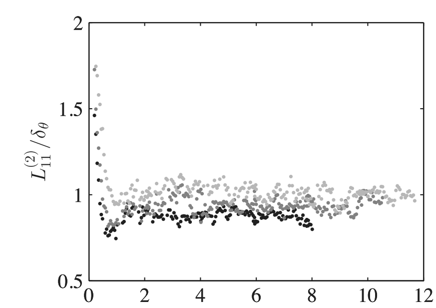

Fig. 6 Evolution of $L_{11}^{(2)}/\delta_\theta$ along the mixing layer, $M_j = 1.10$; • $M_f = 0.05$, • $M_f = 0.22$, • $M_f = 0.39$.

Table 5 Ratios between the growth rates of $L_{ii}^{(j)}$ and those of δ_θ as a function of M_j and M_f

	$[\mathrm{d}L_{11}^{(1)}/\mathrm{d}x]/[\mathrm{d}\delta_\theta/\mathrm{d}x]$			$[\mathrm{d}L_{11}^{(2)}/\mathrm{d}x]/[\mathrm{d}\delta_\theta/\mathrm{d}x]$			$[\mathrm{d}L_{22}^{(1)}/\mathrm{d}x]/[\mathrm{d}\delta_\theta/\mathrm{d}x]$		
M_f	0.05	0.22	0.39	0.05	0.22	0.39	0.05	0.22	0.39
$M_j = 1.10$	1.76	1.93	1.99	0.83	0.97	0.98	0.56	0.52	0.65
$M_j = 1.15$	1.95	2.28	2.40	0.89	1.01	1.15	0.66	0.78	0.72

several images recorded at different axial locations.) When M_f is increased, the shock-cell structure is longer, meaning that it includes more shock cells (which is different from the shock-cell lengthening presented later). This effect was already stated by Sarohia [14], and can also be observed on the static-pressure measurements by Rask et al. [19] and Norum and Brown [18]. In the latter reference, the flight effect is quite spectacular at the maximum M_f value of 0.9, with more than twice as many shock cells as for $M_f = 0$. However, this phenomenon is not very pronounced in the measurements by Norum and Shearin [17], for reasons which will be put forward in Sec. IV.E.

The stretching of the shock-cell structure can be explained by the reduced growth of the mixing layer in flight, emphasized in Sec. III. B. It induces a lengthening of the potential core, particularly visible in Fig. 1, and of the supersonic core. This situation naturally entails a stretching of the shock-cell pattern, because the turbulent mixing with the ambient medium, or equivalently the growth of the mixing layer, is responsible for the attenuation of the shock-cell pattern [39,40].

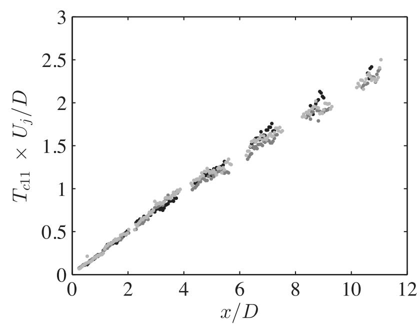

Fig. 7 Evolution of $T_{c11} \times U_j/D$ along the mixing layer for $M_j = 1.10$; • $M_f = 0.05$, • $M_f = 0.22$, • $M_f = 0.39$.

B. Shock-Cell Length Prediction for BBSAN Modeling

The flight effects on the shock-cell length are studied in two separate paragraphs. Here, the length of the shock cells relevant for BBSAN is considered. To that end, the results obtained with the screech-suppressing notched nozzle are analyzed.

The positions of the shock-cell ends have been deduced from the schlieren pictures shown in Fig. 8, and they are displayed in Fig. 9b. Some uncertainty estimates are shown for $M_f = 0$ by the vertical bars; they remain valid for the other values of M_f. The uncertainty increases for the downstream cells because of their fuzzy character on the mean pictures. For each value of M_f, the individual cell length decreases when moving downstream, which is a typical feature of shock-cell patterns (refer to [11], for instance). This decrease is approximately linear, and straight lines, also shown in Fig. 9, have been fitted to each data set. For $M_f = 0.39$, the two first cells are left out of the fit, because they are notably shorter. The fact that these cells behave differently from the ones further downstream can be interpreted as an effect of the initial conditions; see Sec. IV.E. For $M_j = 1.15$, the slopes are −0.040, −0.033, and −0.031 βD per cell for $M_f = 0$, 0.22, and 0.39, respectively. Hence, the decrease in cell length is slowed down with secondary flow, which reflects the well-known shock-cell lengthening in flight [13,17,40–42]. It seems, however, incorrect to state, as it has been done in the past, that only the downstream shock cells are affected by flight: from Fig. 9, it is visible that the stretching is continuous over the entire pattern. Similar results obtained for $M_j = 1.10$ are presented in Fig. 9a. The slopes of the linear fits are −0.033, −0.028, and −0.026 βD per cell for $M_f = 0$, 0.22, and 0.39, respectively. This case is remarkably similar to the $M_j = 1.15$ jet.

The shock-cell lengthening is the product of several factors. The extension of the Prandtl–Pack vortex-sheet model [43,44] by Morris [41] shows that it is already a result of the modified boundary conditions existing near the exit of the supersonic jet. Furthermore, the more detailed analysis proposed by Michalke [40] demonstrates that, for a finite shear-layer thickness, the cell length is reduced when

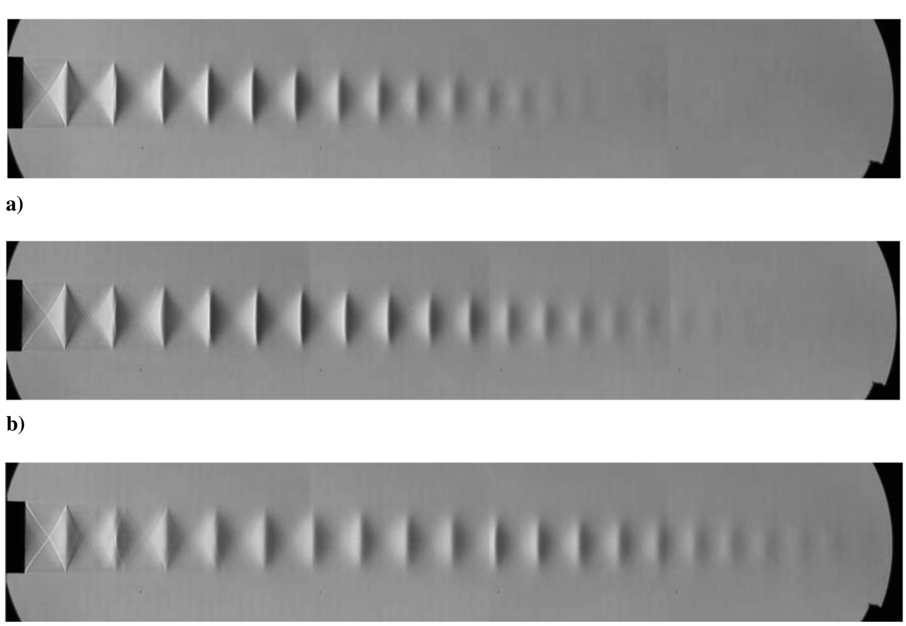

a)

b)

c)

Fig. 8 Mean schlieren images, $M_j = 1.15$ (notched nozzle); a) $M_f = 0$, b) $M_f = 0.22$, and c) $M_f = 0.39$.

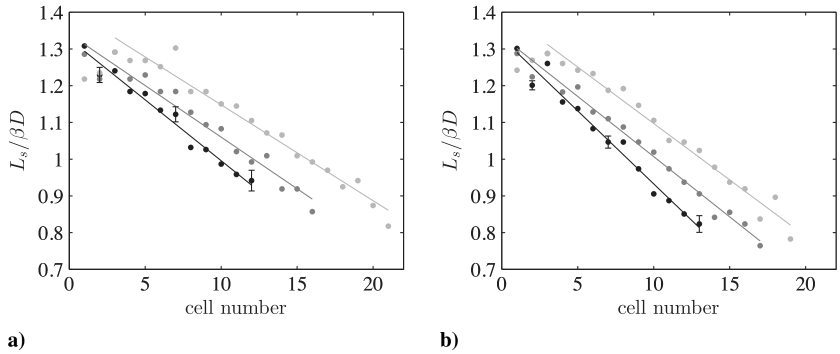

Fig. 9 $L_s/\beta D$ **for each shock cell; a)** $M_j = 1.10$, **b)** $M_j = 1.15$; • $M_f = 0$, • $M_f = 0.22$, • $M_f = 0.39$.

the thickness is increased. Thus, the thinner shear layer induced by flight (see Sec. III.B) also entails a shock-cell lengthening.

The data reduction shown in Fig. 9 could be used to express an empirical relation of the shock-cell lengthening induced by flight, which would be of interest for BBSAN modeling. Such a formula has been proposed by Tam [42] in the extension of his BBSAN theory to flight. It reads

$$\overline{L_s^f} = \overline{L_s^g}(1 + 0.625M_f) \tag{8}$$

in which $\overline{L_s^f}$ and $\overline{L_s^g}$ are the mean shock-cell lengths in flight and on the ground ($M_f = 0$), respectively. In the current state of knowledge, however, it does not seem possible to know which shock cells have to be considered to compute the mean. Indeed, it is still unclear which cells are responsible for BBSAN emission. It is believed that the downstream ones are more important in that respect [45,46], but considering the significant stretching of the shock-cell pattern in flight, this approximate location is not precise enough for high values of M_f. Depending on which part of the pattern is chosen, the mean shock-cell length can significantly vary (although the present data lead to slopes which are constantly smaller than the factor 0.625 of Eq. (8) [8]). A more precise knowledge on BBSAN source location, in particular under flight conditions, is needed to conclude on a mean shock-cell length evolution with M_f from Fig. 9.

C. Shock-Cell Length Prediction for Screech Modeling

A mean length of the cells responsible for screech is now estimated in analyzing data obtained with the screeching plain nozzle. Only the processed data are shown here.

It is known that screech is emitted by the upstream shock cells [47,48], and the sizes of the second to fifth cells are averaged here, for each value of M_f (assuming thus that the screech source does not slide downstream in flight). The results are shown in Fig. 10, in which the present data come from schlieren visualizations and pressure measurements. The predictions of the vortex-sheet model by Morris [41] are included, as well as those of Tam's empirical formula (8). The shock spacing predicted by these models for $M_f = 0$ is matched with the measured data to compare only the flight-induced lengthening. When they correspond to our jet conditions, data of Norum and Shearin [17] are also shown; they represent the mean length calculated over the same shock-cell interval. The present data have been obtained from pressure traverses and schlieren visualizations. This allows an uncertainty on the mean length to be estimated.

The mean length deduced from [17] is smaller than the one here, as well as its increase with M_f. Moreover, no model delivers a good comparison with the experimental values. This is not very surprising. Firstly, Morris's vortex-sheet model [41] should be valid close to the nozzle exit, where the shear layer is very thin, while here, the considered shock cells extend a few diameters downstream of the exit. Secondly, Tam's formula (8) has been designed for predicting the evolution in flight of the length of the downstream shock cells responsible for BBSAN, while here, the first few cells are isolated. It can be noted that these explanations are coherent with the slope relations between the present data and the models. Using a linear formulation for the cell lengthening, reading

$$\overline{L_s^f} = \overline{L_s^g}(1 + aM_f) \tag{9}$$

the values $a = 0.12$ and 0.22 are found from the present data for $M_j = 1.10$ and 1.15, respectively. Other measurements at $M_j = 1.35$ and 1.50, not presented here, show that a increases with M_j.

D. Flight Effects on the Shock-Cell Strength

Static-pressure profiles have been measured in jets exhausting from the (nominally screeching) plain nozzle. As discussed in [21], screech induces a quicker damping of the shock-cell structure. However, the shock-cell strength should be approximately the same with the plain and the screech-suppressing notched nozzle for the cells existing in both jets, as it can be seen in the latter reference. A reason thereof is that screech is usually suppressed by the disruptions brought about by the probe, at least in the upstream part of the flow. Furthermore, the results presented in the following are in full agreement with shock-cell-strength estimates based on PIV data obtained with the notched nozzle [8].

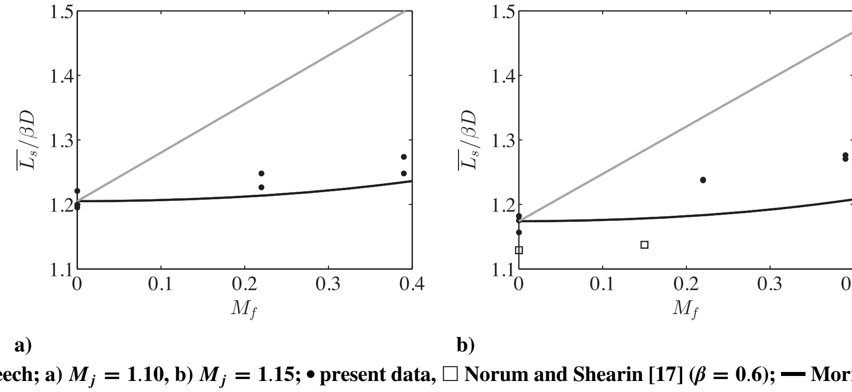

Fig. 10 $\overline{L_s}/\beta D$ **for screech; a)** $M_j = 1.10$, **b)** $M_j = 1.15$; **• present data, □ Norum and Shearin [17] ($\beta = 0.6$); ━ Morris's model [41], ━ Eq. (8).**

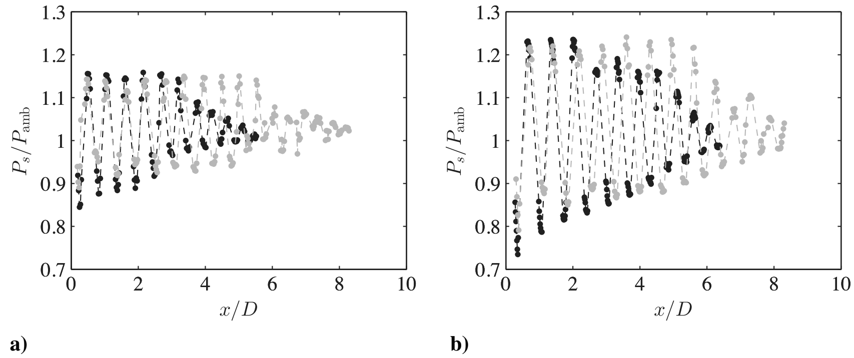

Fig. 11 Centerline static-pressure profiles; a) $M_j = 1.10$, b) $M_j = 1.15$; • $M_f = 0$, • $M_f = 0.39$.

The static-pressure profiles were acquired in two steps. A first coarse traverse was performed to localize the ends of the expansion (pressure minima) and compression regions (pressure maxima). Then, a second finer traverse was done, in which the measurement points were concentrated around the extrema of the coarse curve. So, the pressure extrema are better caught and the strength estimations are more accurate. Such finer traverses are shown in Fig. 11 on the jet centerline for both values of M_j investigated. (The data for $M_f = 0.22$ are not shown here for clarity of the figure; the measured pressures are anyway very close to the case $M_f = 0$.) Off-axis measurements, not shown here, lead to the same conclusions as the ones established in the following [8].

The shock-cell strength can be expressed by $P_{\max}/P_{\min} - 1$ [49], with $P_{\max}$ ($P_{\min}$) the maximum (minimum) pressure in each cell. The strength calculated from the profiles displayed in Fig. 11 is shown in Fig. 12 for $M_j = 1.10$ and 1.15. Quite consistent trends are obtained for both jets. The small effect induced by a low flight speed is reminiscent of Norum and Shearin's results [15]. From $M_f = 0.22$ to 0.39, the pattern is markedly longer, which is associated with a decrease in the attenuation rate of the cell strength when moving downstream. Furthermore, the first shock cells are weaker at $M_f = 0.39$.

Usually, it is accepted that flight has no effect on the shock-cell strength [17,42]. However, a quantitative analysis of the data of Norum and Shearin [17] and Norum and Brown [18] shows that their results also present a decrease in the strength of the initial shock cells accompanied by an increase in the strength of the downstream cells, albeit not as clear as it is here.

The flight effect on the shock-cell strength observed from the present data is actually expected and can be related, together with the effect on the shock-cell length, to the flight-induced lengthening of the entire pattern. The physical causes of the latter phenomenon are known and they have been given in Sec. IV.A. The reason for the decrease of the strength of the upstream shock cells in flight is, however, still not clear.

Some clues that can explain the discrepancies observed with the literature are discussed in the next section.

E. Influence of the Experimental Conditions

To begin with, it has been mentioned in Sec. IV.D that some of the discrepancies with the literature partly vanished upon a detailed analysis. Still, several factors can contribute to a quantitative disagreement between the trends observed.

The initial conditions, and in particular the outer boundary-layer thickness, have an effect on the mean flow of supersonic jets in flight, next to the influence on the turbulence properties mentioned earlier. Sarohia [14] found in particular that the outer boundary-layer thickness affects the shock-cell length in flight. The results presented in Sec. IV.B also corroborate this conclusion: the peculiar behavior of the length of the first two cells at $M_f = 0.39$ occurs inside a distance of $2D$ downstream of the exit, which is also the range in which initial conditions had an effect on turbulence levels (see Sec. III.A).

In the facility of Norum and Shearin [17] and Norum and Brown [18], the primary jet exhausted 14 and 10 in. downstream of the secondary-stream exit plane, respectively. In the present study, both jets have the same exit plane. Hence, variations in the external boundary-layer thickness are expected, which should also be affected by the external geometry of the primary-jet nozzle. Assuming that this boundary layer is thinner in the present experiment, it is expected that our results show a larger flight effect than those studies, in which the supersonic jet should be shielded on a longer distance by the outer boundary layer.

But, like for the evolution of the turbulence levels in flight shown in Sec. III.A, it does not seem probable that the external boundary-layer thickness affects the entire shock-cell pattern. Another factor that can lead to discrepancies between different studies is the screech or probe noise that may appear during the static-pressure measurements. Strong levels of tonal noise during the acquisitions, be it screech or probe noise, lead inevitably to a quick attenuation in the measured shock-cell structure. An example of such a case is shown in Fig. 13 for $M_j = 1.35$ (plain nozzle). In our facility, screech is reinforced in simulated flight at this operating condition [20], and it is clear that the measured shock-cell pattern is not stretched at all in this case, in opposition to what was observed for $M_j = 1.10$ and 1.15. The abrupt damping of some patterns presented in [17] may be explained this

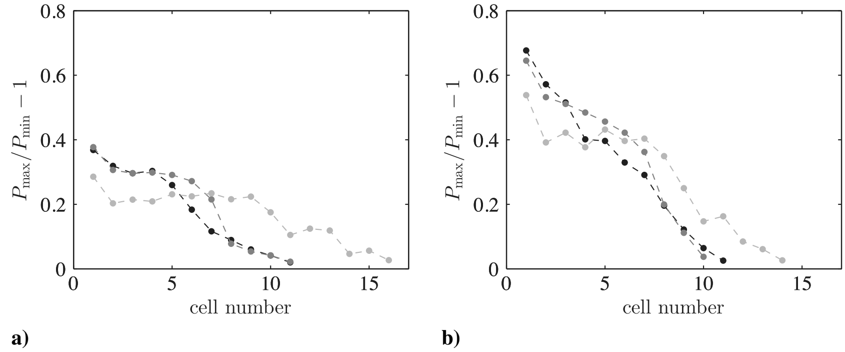

Fig. 12 Shock-cell strength on the jet centerline; a) $M_j = 1.10$, b) $M_j = 1.15$; • $M_f = 0$, • $M_f = 0.22$, • $M_f = 0.39$.

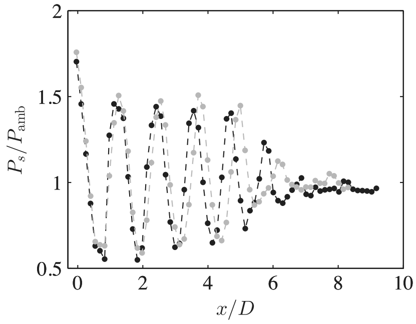

Fig. 13 Centerline static-pressure profiles at $M_j = 1.35$; • $M_f = 0$, • $M_f = 0.39$.

way. For the results shown in Sec. IV.D, however, the strength of the screech tone or the probe tone, when present, is approximately the same whatever the value of M_f, which permits a safe analysis of the flight effect to be conducted. Also, it might occur that the modal behavior of screech disrupts the measurements. Such a case can be seen in Fig. 4 of Norum and Brown [18], in which a mode jump was responsible for the strong shortening of the cell pattern between $M_f = 0.3$ and 0.45.

V. Conclusions

The flight effects on the properties of the mixing layer and the shock-cell system of slightly underexpanded supersonic jets have been studied experimentally. Most of the results have been obtained with a screech-suppressing nozzle to better simulate the conditions arising in air transport.

The turbulence levels have been found constant in flight when the rms velocity fluctuations are nondimensioned by the velocity difference between the high-speed and low-speed flows. Because of the reduced mean shear across the mixing layer with external flow, the linear growth of its thickness is slowed down when the flight Mach number M_f is increased. Accordingly, the growth of the turbulence length scales is slower in flight. The ratios of the growth rates of these length scales to the layer thickness nonetheless show a consistent tendency to increase with flight velocity. Finally, an independence of the integral timescales in the convected frame on M_f has been found.

It has been observed that the shock-cell pattern is lengthened in flight, meaning that more shock cells are visible. This is due to the stretching of the entire flow coming from the reduced mixing-layer growth rates. A concomitant effect is the lengthening of the individual shock cells. In particular, it has been shown that, in a screech-suppressed jet, the length of the individual shock cells decreases approximately linearly with the cell number for all values of M_f investigated, and that the rate of decrease is reduced when M_f is raised. Whereas it appears difficult to deduce a mean shock-cell length for broadband shock-associated noise modeling purposes, such a scale has been calculated for screech modeling in averaging the length of the initial cells of a screeching jet. A roughly linear variation of this mean shock spacing with M_f has been found, with a coefficient depending on the supersonic-jet Mach number M_j. The evolution of the shock-cell strength has been obtained by detailed pressure measurements in the jet plume. A limited effect of flight has been identified for $M_f = 0.22$, whereas the stretching of the shock-cell pattern was clearer at the highest value of M_f tested (0.39), in the form of a reinforcement of the downstream shock cells. It was accompanied by a decrease in the strength of the first shock cells, for still unknown reasons.

Two factors have been isolated in this study, which ought to be carefully controlled in future experiments. One is the appearance of disruptive screech or probe tones during the pressure measurements, whereas the other is the thickness of the boundary layer developing on the outer side of the nozzle of the supersonic jet. These two features are thought to be the cause of the discrepancies between studies focusing on the flight effect on the mean flow or the turbulence of supersonic jets in flight.

Whereas the effect of screech or probe tones on the flow is rather well known [21], it would be of interest to perform measurements with varying external boundary-layer thickness in a single facility to elucidate the effect of this feature. Anyway, it is suggested that, while designing a flight experiment, care should be taken of the conditions arising in the full-scale problem that one aims at reproducing. The external boundary layer should ultimately represent the one developing on the engine cowl.

Acknowledgments

The authors wish to thank Airbus Operations SAS (Mauro Porta) and Snecma (Guillaume Bodard) for their joint financial support, as well as Jean-Michel Perrin and Nathalie Grosjean for their help in setting up the experiment and the particle image velocimetry measurement system.

References

[1] Drevet, P., Duponchel, J. P., and Jacques, J. R., "The Effect of Flight on Jet Noise as Observed on the Bertin Aérotrain," *Journal of Sound and Vibration*, Vol. 54, No. 2, 1977, pp. 173–201. doi:10.1016/0022-460X(77)90022-0

[2] Michalke, A., and Michel, U., "Prediction of Jet Noise in Flight from Static Tests," *Journal of Sound and Vibration*, Vol. 67, No. 3, 1979, pp. 341–367. doi:10.1016/0022-460X(79)90541-8

[3] Morris, P. J., "Turbulence Measurements in Subsonic and Supersonic Axisymmetric Jets in a Parallel Stream," *AIAA Journal*, Vol. 14, No. 10, 1976, pp. 1468–1475. doi:10.2514/3.61485

[4] Tanna, H. K., and Morris, P. J., "In-Flight Simulation Experiments on Turbulent Jet Mixing Noise," *Journal of Sound and Vibration*, Vol. 53, No. 3, 1977, pp. 389–405. doi:10.1016/0022-460X(77)90422-9

[5] Larson, R. S., McColgan, C. J., and Packman, A. B., "Jet Noise Source Modification due to Forward Flight," *AIAA Journal*, Vol. 16, No. 3, 1978, pp. 225–232. doi:10.2514/3.60881

[6] Panda, J., and Seasholtz, R. G., "Measurement of Shock Structure and Shock–Vortex Interaction in Underexpanded Jets Using Rayleigh Scattering," *Physics of Fluids*, Vol. 11, No. 12, 1999, pp. 3761–3777. doi:10.1063/1.870247

[7] André, B., Castelain, T., and Bailly, C., "Experimental Exploration of Underexpanded Supersonic Jets," *Shock Waves*, Vol. 24, No. 1, 2014, pp. 21–32. doi:10.1007/s00193-013-0457-4

[8] André, B., "Étude expérimentale de l'effet du vol sur le bruit de choc de jets supersoniques sous-détendus," Ph.D. Dissertation, École Centrale de Lyon, Écully, France, 2012.

[9] Powell, A., "On the Mechanism of Choked Jet Noise," *Proceedings of the Physical Society, Section B*, Vol. 66, No. 12, 1953, pp. 1039–1056. doi:10.1088/0370-1301/66/12/306

[10] Raman, G., "Advances in Understanding Supersonic Jet Screech: Review and Perspective," *Progress in Aerospace Sciences*, Vol. 34, Nos. 1–2, 1998, pp. 45–106. doi:10.1016/S0376-0421(98)00002-5

[11] Harper-Bourne, M., and Fisher, M. J., "The Noise from Shock Waves in Supersonic Jets," AGARD, CP 131, 1973.

[12] Tam, C. K. W., and Tanna, H. K., "Shock Associated Noise of Supersonic Jets from Convergent–Divergent Nozzles," *Journal of Sound and Vibration*, Vol. 81, No. 3, 1982, pp. 337–358. doi:10.1016/0022-460X(82)90244-9

[13] Bryce, W. D., and Pinker, R. A., "The Noise from Unheated Supersonic Jets in Simulated Flight," *4th Aeroacoustics Conference*, AIAA Paper 1977-1327, Oct. 1977.

[14] Sarohia, V., "Some Flight Simulation Experiments on Jet Noise from Supersonic Underexpanded Flows," *AIAA Journal*, Vol. 16, No. 7, 1978, pp. 710–716. doi:10.2514/3.60958

[15] Norum, T. D., and Shearin, J. G., "Effects of Simulated Flight on the Structure and Noise of Underexpanded Jets," NASA TP 2308, 1984.

[16] Norum, T. D., and Shearin, J. G., "Shock Noise from Supersonic Jets in Simulated Flight to Mach 0.4," *10th Aeroacoustics Conference*, AIAA Paper 1986-1945, July 1986.

[17] Norum, T. D., and Shearin, J. G., "Shock Structure and Noise of Supersonic Jets in Simulated Flight to Mach 0.4," NASA TP 2785, 1988.

[18] Norum, T. D., and Brown, M. C., "Simulated High Speed Flight Effects on Supersonic Jet Noise," *15th Aeroacoustics Conference*, AIAA Paper 1993-4388, Oct. 1993.

[19] Rask, O., Kastner, J., and Gutmark, E., "Understanding How Chevrons Modify Noise in a Supersonic Jet with Flight Effects," *AIAA Journal*, Vol. 49, No. 8, 2011, pp. 1569–1576. doi:10.2514/1.J050628

[20] André, B., Castelain, T., and Bailly, C., "Experimental Study of Flight Effects on Screech in Underexpanded Jets," *Physics of Fluids*, Vol. 23, Dec. 2011, Paper 126102-1–126102-14. doi:10.1063/1.3671735

[21] André, B., Castelain, T., and Bailly, C., "Broadband Shock-Associated Noise in Screeching and Non-Screeching Underexpanded Supersonic Jets," *AIAA Journal*, Vol. 51, No. 3, 2013, pp. 665–673. doi:10.2514/1.J052058

[22] Pinckney, S. Z., "A Short Static-Pressure Probe Design for Supersonic Flow," NASA TN D-7978, 1975.

[23] Norum, T. D., and Seiner, J. M., "Measurements of Mean Static Pressure and Far Field Acoustics of Shock Containing Supersonic Jets," NASA TM-84521, 1982.

[24] Raffel, M., Willert, C. E., Wereley, S. T., and Kompenhans, J., *Particle Image Velocimetry — A Practical Guide*, 2nd ed., Springer, Berlin, 2007, pp. 49–52.

[25] Coleman, H. W., and Steele, W. G., *Experimentation and Uncertainty Analysis for Engineers*, John Wiley and Sons, New York, 1989, p. 48.

[26] Edgington-Mitchell, D., Oberleithner, K., Honnery, D. R., and Soria, J., "Coherent Structure and Sound Production in the Helical Mode of a Screeching Axisymmetric Jet," *Journal of Fluid Mechanics*, Vol. 748, 2014, pp. 822–847. doi:10.1017/jfm.2014.173

[27] Mitchell, D. M., Honnery, D. R., and Soria, J., "Near-Field Structure of Underexpanded Elliptic Jets," *Experiments in Fluids*, Vol. 54, July 2013, pp. 1578-1–1578-13. doi:10.1007/s00348-013-1578-3

[28] Nouri, J. M., and Whitelaw, J. H., "Flow Characteristics of an Underexpanded Jet and Its Application to the Study of Droplet Breakup," *Experiments in Fluids*, Vol. 21, No. 4, 1996, pp. 243–247. doi:10.1007/BF00190673

[29] Ragni, D., Schrijer, F., van Oudheusden, B. W., and Scarano, F., "Particle Tracer Response Across Shocks Measured by PIV," *Experiments in Fluids*, Vol. 50, No. 1, 2011, pp. 53–64. doi:10.1007/s00348-010-0892-2

[30] André, B., Castelain, T., and Bailly, C., "Investigation of the Mixing Layer of Underexpanded Supersonic Jets by Particle Image Velocimetry," *International Journal of Heat and Fluid Flow*, Vol. 50, No. 3, 2014, pp. 188–200. doi:10.1016/j.ijheatfluidflow.2014.08.004

[31] Goebel, S. G., and Dutton, J. C., "Experimental Study of Compressible Turbulent Mixing Layers," *AIAA Journal*, Vol. 29, No. 4, 1991, pp. 538–546. doi:10.2514/3.10617

[32] Sarohia, V., and Massier, P. F., "Effects of External Boundary-Layer Flow on Jet Noise in Flight," *AIAA Journal*, Vol. 15, No. 5, 1977, pp. 659–664. doi:10.2514/3.60676

[33] Troutt, T. R., and McLaughlin, D. K., "Experiments on the Flow and Acoustic Properties of a Moderate-Reynolds-Number Supersonic Jet," *Journal of Fluid Mechanics*, Vol. 116, 1982, pp. 123–156. doi:10.1017/S0022112082000408

[34] Sarohia, V., "Flight Effects on Subsonic Jet Noise," *5th Aeroacoustics Conference*, AIAA Paper 1979-616, March 1979.

[35] Papamoschou, D., and Roshko, A., "The Compressible Turbulent Shear Layer: An Experimental Study," *Journal of Fluid Mechanics*, Vol. 197, 1988, pp. 453–477. doi:10.1017/S0022112088003325

[36] Smits, A. J., and Dussauge, J. P., *Turbulent Shear Layers in Supersonic Flow*, 2nd ed., Springer, New York, 2006, pp. 155, 158.

[37] Tam, C. K. W., "Stochastic Model Theory of Broadband Shock-Associated Noise from Supersonic Jets," *Journal of Sound and Vibration*, Vol. 116, No. 2, 1987, pp. 265–302. doi:10.1016/S0022-460X(87)81303-2

[38] Fleury, V., Bailly, C., Jondeau, E., Michard, M., and Juvé, D., "Space–Time Correlations in Two Subsonic Jets Using Dual Particle Image Velocimetry Measurements," *AIAA Journal*, Vol. 46, No. 10, 2008, pp. 2498–2509. doi:10.2514/1.35561

[39] Tam, C. K. W., Jackson, J. A., and Seiner, J. M., "A Multiple-Scales Model of the Shock-Cell Structure of Imperfectly Expanded Supersonic Jets," *Journal of Fluid Mechanics*, Vol. 153, 1985, pp. 123–149. doi:10.1017/S0022112085001173

[40] Michalke, A., "On the Effect of External Flow and Shear-Layer Thickness on the Expansion Cells of Under-Expanded Supersonic Circular Jets," *European Journal of Mechanics, B/Fluids*, Vol. 11, No. 3, 1992, pp. 363–381.

[41] Morris, P. J., "A Note on the Effect of Forward Flight on Shock Spacing in Circular Jets," *Journal of Sound and Vibration*, Vol. 122, No. 1, 1988, pp. 175–177. doi:10.1016/S0022-460X(88)80014-2

[42] Tam, C. K. W., "Broadband Shock-Associated Noise from Supersonic Jets in Flight," *Journal of Sound and Vibration*, Vol. 151, No. 1, 1991, pp. 131–147. doi:10.1016/0022-460X(91)90656-5

[43] Prandtl, L., "Über die stationären Wellen in einem Gasstrahl," *Physikalische Zeitschrift*, Vol. 5, No. 19, 1904, pp. 599–601.

[44] Pack, D. C., "A Note on Prandtl's Formula for the Wave-Length of a Supersonic Gas Jet," *Quarterly Journal of Mechanics and Applied Mathematics*, Vol. 3, No. 2, 1950, pp. 173–181. doi:10.1093/qjmam/3.2.173

[45] Norum, T. D., and Seiner, J. M., "Broadband Shock Noise from Supersonic Jets," *AIAA Journal*, Vol. 20, No. 1, 1982, pp. 68–73. doi:10.2514/3.51048

[46] Seiner, J. M., and Yu, J. C., "Acoustic Near-Field Properties Associated with Broadband Shock Noise," *AIAA Journal*, Vol. 22, No. 9, 1984, pp. 1207–1215. doi:10.2514/3.8762

[47] Lee, B. H. K., and Westley, R., "Effective Axial Source Distribution in a Choked Screech Jet," *10th Aerospace Sciences Meeting*, AIAA Paper 1972-159, Jan. 1972.

[48] Umeda, Y., and Ishii, R., "On the Sound Sources of Screech Tones Radiated from Choked Circular Jets," *Journal of the Acoustical Society of America*, Vol. 110, No. 4, 2001, pp. 1845–1858.

[49] Seiner, J. M., and Norum, T. D., "Aerodynamic Aspects of Shock Containing Jet Plumes," *6th Aeroacoustics Conference*, AIAA Paper 1980-0965, June 1980.

Y. Zhou
Associate Editor